ORIGINAL PAPER

Adsorptive removal of synthetic dye from its aqueous solution by using chitosan-bentonite composite: DFT and experimental studies

Zeynep Mine Şenol[1] · Hüseyin Ertap[2] · Yasmine Fernine[3] · Noureddine El Messaoudi[4]

Abstract

This research investigates the adsorption efficiency of a chitosan-bentonite (Ch–B) composite in removing methyl orange (MO), a common textile dye, from aqueous solutions. The study integrates experimental and theoretical analyses, employing density functional theory (DFT) to gain insights into the molecular interactions between the composite material and MO molecules. The Ch–B composite was characterized using various techniques, including FT-IR spectroscopy, XRD, and SEM–EDX. The experimental results indicate that the Ch–B composite exhibits a high adsorption capacity for MO, with optimal conditions identified for efficient removal. The Langmuir model was found to best fit the experimental data and the adsorption capacity was 117 mg g^{-1}. Adsorption thermodynamics showed that the adsorption process was spontaneous, feasible, and exothermic. DFT calculation results are correlated with experimental findings to confirm theoretical predictions and improve the overall understanding of the adsorption process. Electronic structure calculations reveal the nature of the interactions between the Ch–B composite and MO molecules, including hydrogen bonds and electrostatic forces.

Keywords Chitosan · Bentonite · Composite beads · MO adsorption · DFT calculation · Wastewater treatment

✉ Zeynep Mine Şenol
msenol@cumhuriyet.edu.tr

1 Department of Nutrition and Diet, Faculty of Health Sciences, Sivas Cumhuriyet University, 58140 Sivas, Turkey

2 Department of Physics, Faculty of Science and Letters, Kafkas University, 36100 Kars, Turkey

3 Engineering Laboratory of Organometallic, Molecular Materials and Environment, Sidi Mohamed Ben Abdellah University, 30000 Fez, Morocco

4 Laboratory of Applied Chemistry and Environment, Faculty of Sciences, Ibn Zohr University, 80000 Agadir, Morocco

Introduction

In recent years, the contamination of water bodies by synthetic dyes has emerged as a significant environmental concern. Among various dyes, methyl orange (MO), is a synthetic dye widely used in various industries, particularly in chemistry laboratories, as a pH indicator [1, 2]. In its natural state, it is a bright orange, azoic compound. When dissolved in water, it dissociates into ions, specifically positive hydrogen ions (H^+) and negative organic ions (often denoted as MO^-) due to the acidic nature of the solution [3, 4]. However, the presence of MO in water bodies due to industrial discharges or improper waste disposal can lead to significant environmental concerns [5, 6]. MO imparts a vibrant orange color to the water, making it visually unappealing [7]. This aesthetic degradation can affect the acceptability of water for various purposes. While MO itself is not considered highly toxic to humans, its breakdown products might be harmful, especially if they accumulate in the environment. Additionally, its presence can indicate the potential presence of other harmful pollutants in the water [8, 9]. MO, like many synthetic dyes, can have detrimental effects on aquatic ecosystems [10]. It reduces light penetration into water bodies, affecting photosynthesis in aquatic plants [11]. It can also hinder the growth and development of aquatic organisms, disrupting the natural balance of the ecosystem [12]. Synthetic dyes, including MO, can be resistant to degradation. This persistence in the environment can lead to long-term pollution issues, affecting both surface and groundwater sources [13, 14]. The removal of MO from water sources can be challenging. Conventional water treatment methods may not be highly effective against synthetic dyes, necessitating the use of advanced treatment technologies such as activated carbon adsorption, membrane filtration, or advanced oxidation processes [15–19]. Traditional methods of dye removal often involve complex chemical processes, making them environmentally undesirable [20, 21]. Consequently, there is an urgent need for innovative, sustainable, and eco-friendly solutions to tackle this issue effectively as adsorption on low-cost adsorbents [22, 23].

In response to this challenge, composite materials have garnered attention as promising candidates for efficient dye removal [24]. Among these, chitosan-bentonite composites have emerged as compelling options. Chitosan (Ch), derived from chitin, is a natural biopolymer renowned for its adsorption capabilities, biodegradability, and nontoxicity [25, 26]. Bentonite (B), a clay mineral, is valued for its large surface area and high cation exchange capacity [27, 28]. When combined, these materials create a synergistic effect, enhancing their adsorption properties and making them excellent candidates for the removal of pollutants from aqueous solutions.

This study bridges the gap between theoretical analysis and experimental application by employing density functional theory (DFT) simulations to understand the fundamental mechanisms governing the interaction between the Ch–B composite and MO molecules. Theoretical insights provide valuable information about the adsorption sites, binding energies, and electronic properties, guiding the experimental design. In conjunction with the theoretical

analysis, this research presents a comprehensive experimental investigation. Through a series of controlled experiments, the efficiency of the Ch–B composite in removing MO from aqueous solutions has been meticulously studied. By amalgamating theoretical understanding with practical experimentation, this study aims to provide a holistic perspective on the interaction dynamics between the Ch–B composite and MO. The findings not only contribute to the scientific understanding of dye removal mechanisms but also hold the promise of practical applications in wastewater treatment technologies. In the pursuit of sustainable environmental solutions, this research stands at the forefront, driving innovations in the field of water purification.

Materials and methods

Reagents and instrumentation

Bentonite (B), chitosan (Ch) (medium molecular weight), epichlorohydrin (ECH), and sodium tripolyphosphate (NaTPP) were purchased from Sigma Aldrich. Hydrochloric acid, acetic acid, nitric acid, potassium nitrate, ethyl alcohol, and sodium hydroxide were obtained from Merck.

Instrumentation: The functional groups on the Ch, B, Ch–B, and MO-loaded Ch–B composite were determined using the FT-IR (ATR, ThermoScientificNicolet 6700) technique. The Ch–B and its components were characterized by measurements of scanning electron microscopy (SEM, LEO-EVO 40, Cambridge-İngiltere), and energy-dispersive X-ray spectroscopy (EDX, Bruker-125 eV, Berlin-Almanya). XRD was recorded by the Rigaku RadB-Dmax II. The MO dye concentrations were determined using a UV–vis spectrophotometer (UV-DR-6000; Shimadzu, China) at $\lambda = 460$ nm.

Preparation of Ch–B

To prepare the Ch–B hybrid composite, Ch and B were mixed in 100 mL of a 5% w/v acetic acid solution in a magnetic stirrer at 25 °C for 2 h. Then, 80 mL of a 25% by-weight ECH solution, a cross-linker, was added to this mixture, stirred for 1 h, and left overnight. The next day, the mixture is added dropwise to the NaTPP solution, which is a cross-linker, to form composite beads. The cross-linked Ch–B composite was washed five times with double-distilled water to remove free ECH and NaTPP. Then, the composite beads were filtered and left to dry at 25 °C. After drying, it was ground and stored for use in adsorption studies.

Adsorption experiments

Adsorption experiments were carried out in a batch system using a solution volume of 10 mL and 10 g L^{-1} composite amount at a constant concentration of 500 mg L^{-1} MO, kept at 25 °C for 24 h, and the natural pH value of the

solution was used. Thermodynamic studies at 5, 25, and 40 °C, kinetic studies for 10–1440 min, composite dose in 1–20 g L^{-1} amounts, concentration studies (10–1000 mg L^{-1}) in MO dye concentrations, pH studies were carried out using HCl and NaOH at pH values of 2–12. To find the MO dye concentration at equilibrium, absorbance was measured using a UV–vis spectrophotometer. Equations (1), (2), and (3) were used to estimate adsorption%, Q (mg g^{-1}), and recovery%, respectively.

$$Adsorption\% = \left[\frac{C_i - C_e}{C_i}\right] \times 100 \tag{1}$$

$$Q = \left[\frac{C_i - C_e}{m}\right] \times V \tag{2}$$

$$Recovery\% = \frac{Q_{des}}{Q_{ads}} \times 100 \tag{3}$$

Theoretical research DFT

The use of quantum chemical calculations is of great importance in characterizing various quantum chemical parameters of a molecule, including, but not limited to, the calculated result E_{HOMO} and E_{LUMO} of the MO molecule in the neutral and protonated states, electronegativity (χ), softness (σ), chemical potential (μ), hardness (η), and energy gap (ΔE_{gap}). In the present study, all quantum chemical calculations were performed using Gaussian 09 software [29].

Results and discussion

XRD analysis

The XRD spectra of the Ch, B, Ch–B composite and MO adsorbed Ch–B composite are given in Fig. 1. The XRD spectra showed that Ch, B, Ch–B composite and MO adsorbed Ch–B composite had a polycrystalline structure. The strongest diffraction peaks were observed around $2\theta = 19.9°$, $2\theta = 26.4°$, $2\theta = 26.4°$, and $2\theta = 26.5°$ in the XRD patterns for Ch, B, Ch–B composite, and MO adsorbed Ch–B composite, respectively [30, 31]. According to the XRD spectra of the Ch–B composite and MO-adsorbed Ch–B composite, the peak positions of the MO-absorbed Ch–B composite shifted to larger degrees compared to the peak positions of the Ch–B composite. Also, it was observed that the peak intensity of the strongest peak of MO absorbed Ch–B composite decreased compared to the strongest peak of Ch–B composite. The crystallite size (D) is calculated from the XRD data using the Eq. 4 [32]:
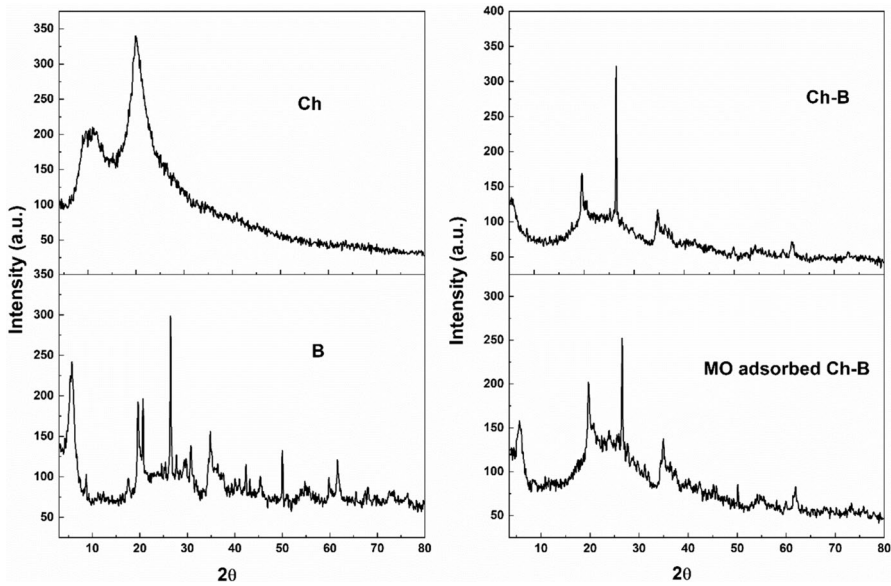
Fig. 1 The XRD spectra of Ch, B, Ch–B, and MO adsorbed Ch–B

$$D = \frac{K\lambda}{(\beta cos\theta)} \tag{4}$$

The average crystallite size (D) and residual strain (ε) were calculated from the diffraction peaks of Ch, B, Ch–B composite, and MO adsorbed Ch–B composite by using equations in the literature [32]. The calculated average crystallite size (D) of Ch, B, Ch–B composite, and MO adsorbed Ch–B composite were found to be 3.0 nm, 35.9 nm, 27.7 nm, and 21.5 nm, respectively. It is seen from XRD results that the average crystallite size of MO adsorbed Ch–B composite decreased compared to Ch–B composite.

FT-IR and SEM–EDX analysis

FT-IR spectra of Ch, B, Ch–B, and MO adsorbed Ch–B are shown in Fig. 2. On the FT-IR spectrum of Ch, The strong band at 3489 cm^{-1} is due to N–H and O–H stretching as well as intramolecular H-bonding. The peak at 2932 cm^{-1} is attributed to C–H stretching vibrations. The peak at 1153 cm^{-1} is the symmetric stretching of the C–O-C bridge. The peak at 1085 cm^{-1} is attributed to the C–O stretching vibration. The peaks at 890 cm^{-1}, 792 cm^{-1}, and 626 cm^{-1} are attributed to C–H bending vibrations [33, 34].

The characteristic peaks of B can be listed as follows. The band at 3640 cm^{-1} is O–H stretching vibrations in Al–OH or Si–OH. The peaks at 3422 cm^{-1} and 1641 cm^{-1} are O–H stretching vibrations in adsorbed water. The peak at 1048 cm^{-1}
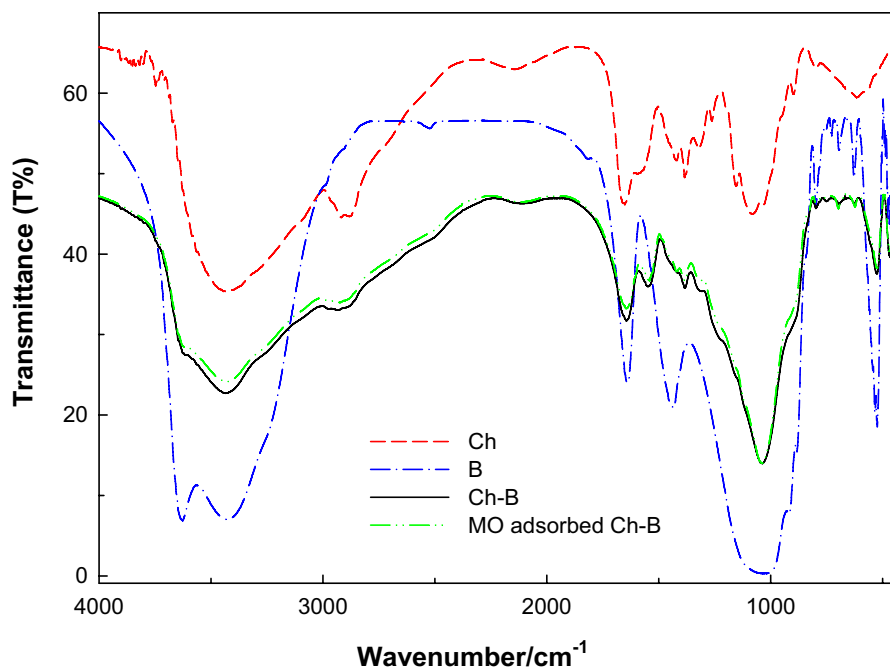
Fig. 2 FT-IR spectra of Ch, B, Ch–B, and MO adsorbed Ch–B composite

is the Si–O stretching vibration. The peaks at 529 cm^{-1} and 461 cm^{-1} are attributed to Al–Si–O and Si–O–Si stretching vibrations, respectively [31, 35]. On the FT-IR spectrum of the Ch–B, C=O, N–H, and C–N peaks are seen at 1648 cm^{-1}, 1543 cm^{-1}, and 1378 cm^{-1}, which are the characteristic peaks of Ch, respectively. Also on the FTIR spectrum of the Ch–B, the characteristic peaks of B, Si–O at 1040 cm^{-1}, Si–O stretches at 7792 cm^{-1}, 754 cm^{-1}, 679 cm^{-1}, and 619 cm^{-1}, are at 524 and 461 cm^{-1}, respectively. Al–Si–O and Si–O–Si stretching vibrations are observed. The peak at 1543 cm^{-1} in the Ch–B composite corresponds to the deformation vibrations of the amino groups of Ch. All these results show that the Ch–B composite, containing functional groups from Ch and B was successfully synthesized. The FT-IR spectrum of MO-adsorbed Ch–B shows that Ch–B has all the compound peaks. The increases and decreases in peak intensities after adsorption confirm the adsorption and electrostatic interactions between MO and Ch–B during the solid–liquid phase interaction.

The SEM images and EDX results of Ch, B, Ch–B composite and MO adsorbed Ch–B composite are given in Fig. 3. The EDX spectra showed that Ch contains Ca, Na, Al, Mg, Si, O; B contains C, O, N; Ch–B composite contains Ca, Na, Al, Mg, Si, O, N and MO adsorbed Ch–B composite contains Ca, Na, Al, Mg, Si, O, N, S, C, respectively. According to EDX results, it was seen that the MO adsorbed Ch–B composite contained S and C, unlike the Ch–B composite. From the SEM images, it was observed that Ch had a porous and smooth surface, while B had a rough surface and irregular edge curves. SEM images of Ch and B are compatible
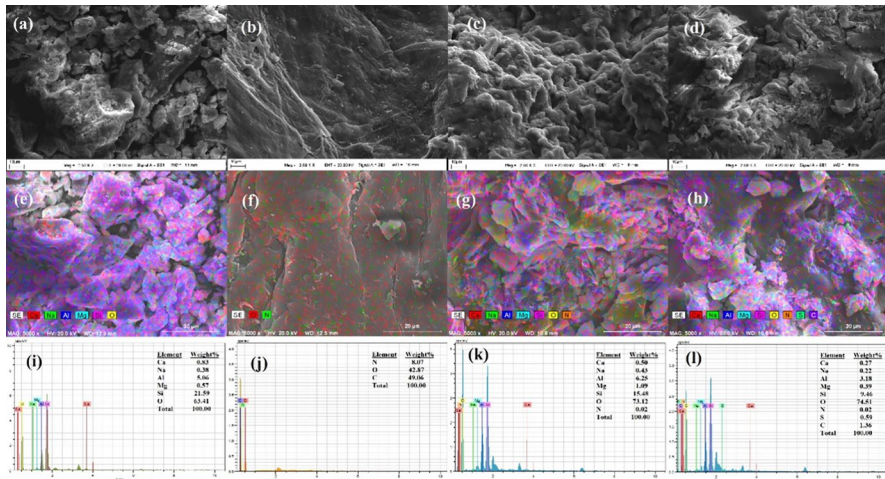
Fig. 3 SEM images of Ch (**a**), B (**b**), Ch–B (**c**), and MO adsorbed Ch–B (**d**), and their corresponding EDX mapping images (**e–h**) and EDX spectra (**i–l**), respectively

with the literature [36, 37]. This images Also, SEM images showed that Ch–B and MO-adsorbed Ch–B composites have a lamellar structure. Also, it was seen in SEM images that there was little change in the surface morphology of the MO-absorbed Ch–B composite compared to the Ch–B composite.

Protonation of MO, pH_{pzc} of Ch–B, and effect of pH

The protonation mechanism of the MO molecule was investigated over a pH range of 0 to 14 using the MarvinSketch software. As illustrated in Fig. 4, the MO molecule exists in both its protonated (a) and neutral (b) forms, and the percentage of protonation sites is also shown. It is noteworthy that the MO molecule exhibits weak basic properties, which promote its protonation in acidic media. Furthermore, the presence of heteroatoms in the molecule further highlights its strong inclination towards protonation in solution. Figure 4 depicts the distribution ratio of each species as a function of pH, revealing that only one predominant form (MO–H^+) was present at 100% at pH=0 [38], which indicates the molecule's high affinity for protons in strongly acidic conditions.

Figure 5 depicts the impact of pH (2.0–12.0) on the adsorption capacity of MO molecules by the Ch–B adsorbent. This investigation keeps the other crucial parameters constant ([MO]$_0$:500 mg L^{-1}, Ch–B dosage: 10 g L^{-1}, contact time: 24 h, temperature: 25 °C). The adsorption capacity of MO molecules increases (from 29.4 to 71.9 mg g^{-1}) as the pH rises (from pH:2.0 to pH:8.0), after pH 8, the adsorption capacity of MO decreases.

The point of zero charge of the Ch–B composite was determined using the solid addition method. In this method, 10 mL of KNO_3 solution at 0.1 mol L^{-1} concentration was transferred to a 10 mL polypropylene tube. Solutions with different initial pH (pH$_i$) between pH: 2.0 and pH: 12.0 were prepared by adding
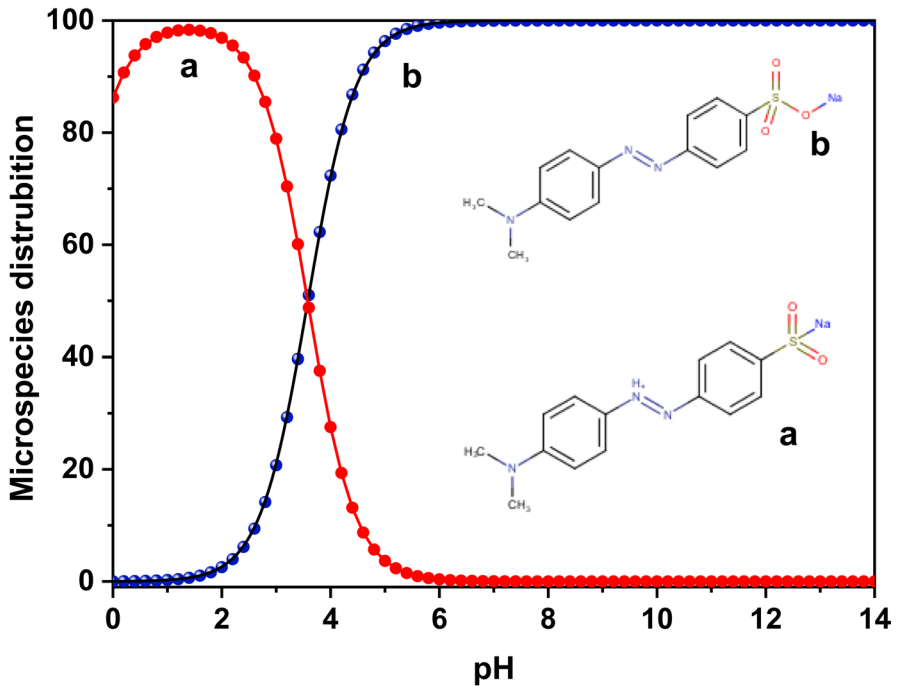
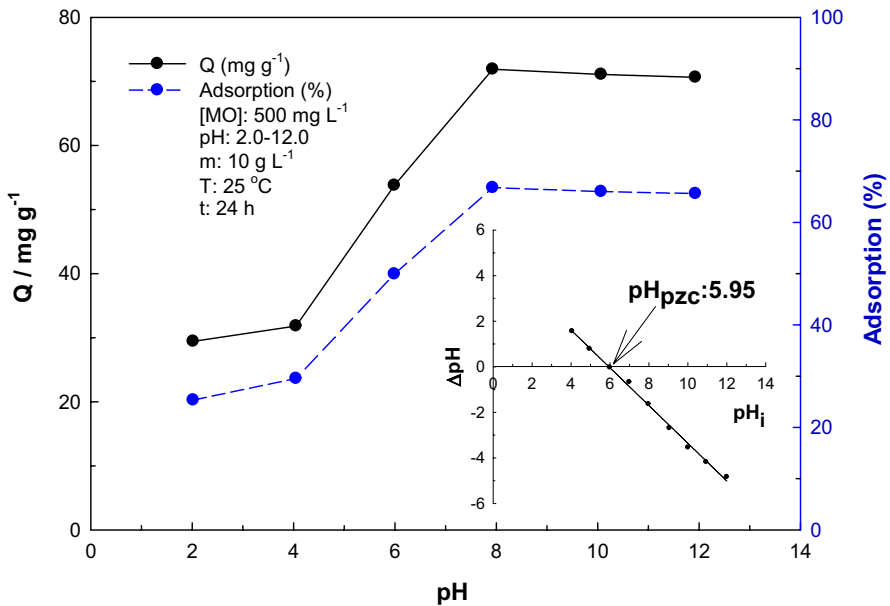**Fig. 4** Speciation diagram for MO as a function of pH

Fig. 5 Effect of pH on adsorption

0.1 M HCl or 0.1 M NaOH. Then, 100 mg of Ch–B composite was added to the solutions and the pH (pH_f) of the equilibrium solutions was measured after 24 h. The point where ΔpH (pH_f-pH_i) crossed the x-axis plotted against pHi gave the zero charge point (pHpzc). Analysis of Fig. 5 revealed that the pH_{PZC} value of Ch–B was determined to be 5.95. Depending on the pHpzc of the adsorbent, the surface of the Ch–B composite becomes protonated at pH values below 5.95 and negatively charged at pH values exceeding the pHpzc [39, 40]. Consequently, at lower pH levels, the surface of the Ch–B composite carries a positive charge, thereby enhancing the adsorption of MO⁻ through electrostatic forces.

Effect of Ch–B dosage

The observations presented in Fig. 6 demonstrate that increasing the dosage of the adsorbent from 1 to 20 g L^{-1} leads to higher levels of adsorption. It can be seen in the figure that the efficacy of the adsorbent for MO increased at a high dosage of the Ch–B composite, showing that as the Ch–B dose increases from 1 to 20 g L^{-1}, the removal efficiency of the MO also increases from 17.65 to 93.86%, while the adsorption capacity of MO molecules decreases from 304.98 to 27.54 mg g^{-1}. This can be attributed to the larger surface area available for adsorption and the increased number of accessible adsorption sites resulting from higher adsorbent dosages [41, 42].
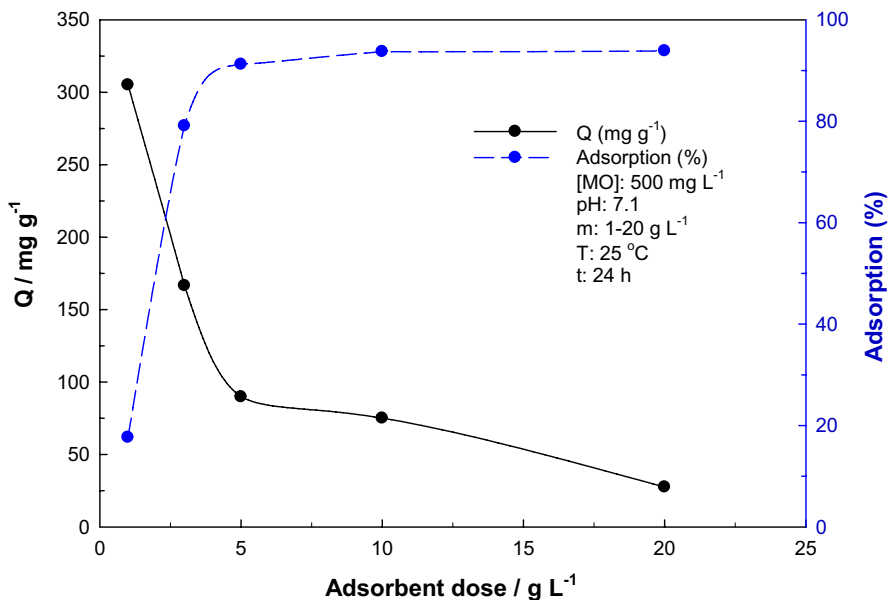

Fig. 6 Effect of Ch–B dosage on adsorption

Adsorption isotherms

The adsorption behavior of MO on Ch–B composite was studied by employing three equilibrium models: Langmuir, Freundlich, and Dubinin-Radushkevich (D–R) isotherm models (Fig. 7), and the parameters derived from the models are presented in Table 1. The Langmuir model fits the MO adsorption data on the Ch–B composite better than the Freundlich and D–R models, according to a comparison of the values of the R^2. This showed that the adsorption process occurred in a monolayer on a homogeneous surface [43]. Therefore, it was thought that homogeneous active centers were dominant on the surface of the Ch–B composite adsorbent. The maximum adsorption capacity (Q_m) was found to be 117 mg g^{-1} from the Langmuir model. The β value, which is the surface heterogeneity factor, was found to be 0.565. This demonstrated that the MO dye adsorption process onto the Ch–B composite was suitable [44]. The adsorption energy was found to be 14.9 kJ mol^{-1}, which indicated that the adsorption process was chemical.

Table 2 lists the performance of the Ch–B composite and other types of adsorbents for the removal of MO from water. By comparison with other adsorbents,
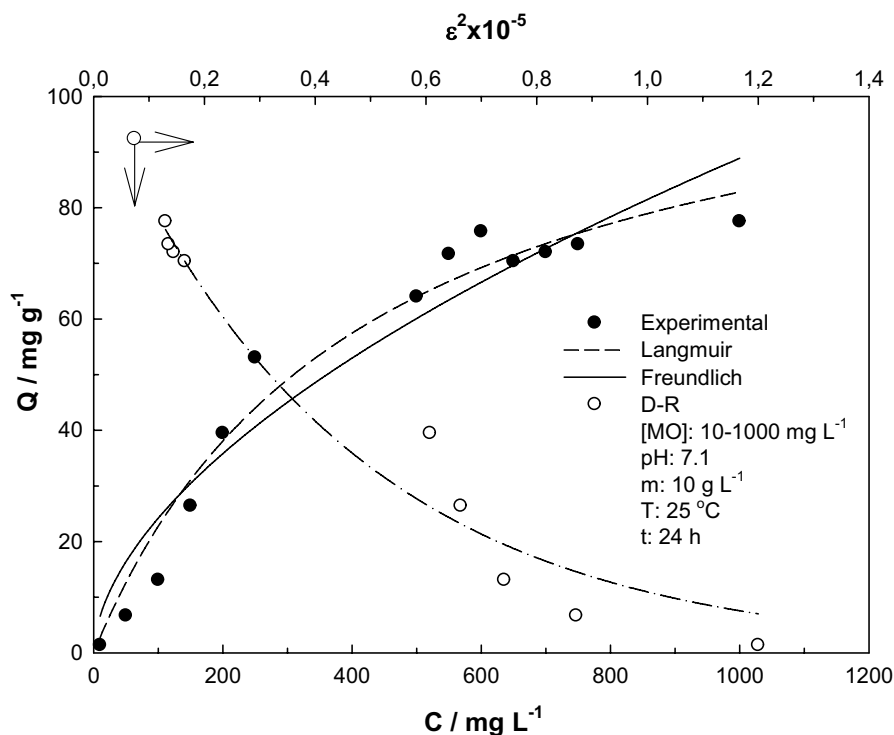
Fig. 7 Experimentally obtained adsorption isotherms MO dye onto Ch–B composite and their compatibility to Langmuir, Freundlich, and D–R models

Table 1 Isotherm parameters for MO adsorbed on Ch–B composite

Isotherm model	Equation	Parameter	Value
Langmuir	$Q = \frac{K_L Q_m C_e}{1 + K_L C_e}$	Q_m (mg g^{-1})	117
		K_L (L mg^{-1})	0.0024
		R^2	0.965
Freundlich	$Q = X_F C_e^{\beta}$	X_F	1.80
		β	0.565
		R^2	0.925
D–R	$Q = X_{DR} e^{-K_{DR}\varepsilon^2}$	X_{DR} (mg g^{-1})	102
	$\varepsilon = RT ln\left(1 + \frac{1}{C_e}\right)$	$-K_{DR} \times 10^9$/mol^2 K J^{-2}	2.23
	$E_{DR} = \left(2K_{DR}\right)^{-0.5}$	E_{DR}/kJ mol^{-1}	14.9
		R^2	0.959

Standard deviation 29.5 mg g^{-1}, standard error 8.52 mg g^{-1}

Table 2 Adsorption performances of different adsorbents for MO removal

Adsorbent	pH	Q_m (mg g^{-1})	References
Coffee waste/cetylpyridinium chloride	3.5	62.5	[45]
Coffee waste/cetyltrimethylammonium bromide	3.5	58.8	[45]
Surfactant-modified pineapple leaf	3.0	47.6	[46]
Biochar from chicken manure	6.5	41.5	[47]
Goethite	3.0	55	[48]
Organic matter-rich clays from Egypt	2.0	41.7	[49]
Poly(N-isopropyl acrylamide)-based ionic hydrogels	–	64.8	[50]
Ionic-liquid-crafted zeolite	–	38	[51]
Mesoporous ZSM-5 zeolite	1.0	25	[52]
Cellulose from *Stipa tenacissina L*	3.7	16.9	[53]
Al-doped CNTs	4.5	69.7	[54]
Co_3O_4 NPs	6.0	46.1	[55]
α-Fe_2O_3 NPs	2.0	28.9	[56]
Amorphous CNTs	3.0	21.5	[57]
Nanoporous carbon	–	18.8	[58]
Nitrogen-doped TiO_2	–	14.1	[59]
γ-Fe_2O_3/2C nanocomposites	4.8	72.7	[60]
Spent tea leaves/polyethyleneimine	3.0	62.1	[61]
NaX/MgO–TiO_2 zeolite	6.5	53.8	[62]
Chitosan-montmorillonite	–	154	[63]
Chitosan composites films	–	173	[64]
Protonated cross-linked chitosan	4.5	89.3	[65]
Chitosan microspheres	–	207	[66]
Cross-linked chitosan/bentonite	–	137	[67]
Ch–B composite	7.1	117	This study

the Ch–B composite was found to have excellent adsorption performance for MO. Therefore, the Ch–B composite can be considered as the desirable adsorbent.

Adsorption kinetics

Adsorption kinetics, finding the contact time between the adsorbent and the adsorbate allows us to have information about what kind of mechanisms play a role in the adsorption of the adsorbate to the surface of the adsorbent [68, 69]. Three common kinetic models used are pseudo-first-order (PFO), pseudo-second-order (PSO), and intra-particular diffusion (IPD) kinetic models Fig. 8. When Fig. 8 is examined, it is seen that the adsorption rate increases as the contact time increases from 10 to 150 min due to the presence of more active centers on the surface of the Ch–B composite adsorbent. After 150 min, it is seen that the adsorption reaches equilibrium in 180 min as the active binding centers on the Ch–B composite surface decrease. Table 3 presents the parameters obtained from fitting the kinetic models. When Table 3 was examined, it was seen that the PSO model (R^2:0.961) showed a higher correlation coefficient than the PFO model (R^2:0.950). In addition, the equilibrium adsorption amount obtained by model fitting (Q_t: 73.4 mg g^{-1}) was more compatible with that obtained experimentally (Q_e: 72.6 mg g^{-1}). This showed that the PSO model had a better fit with the MO dye adsorption process onto the Ch–B composite.
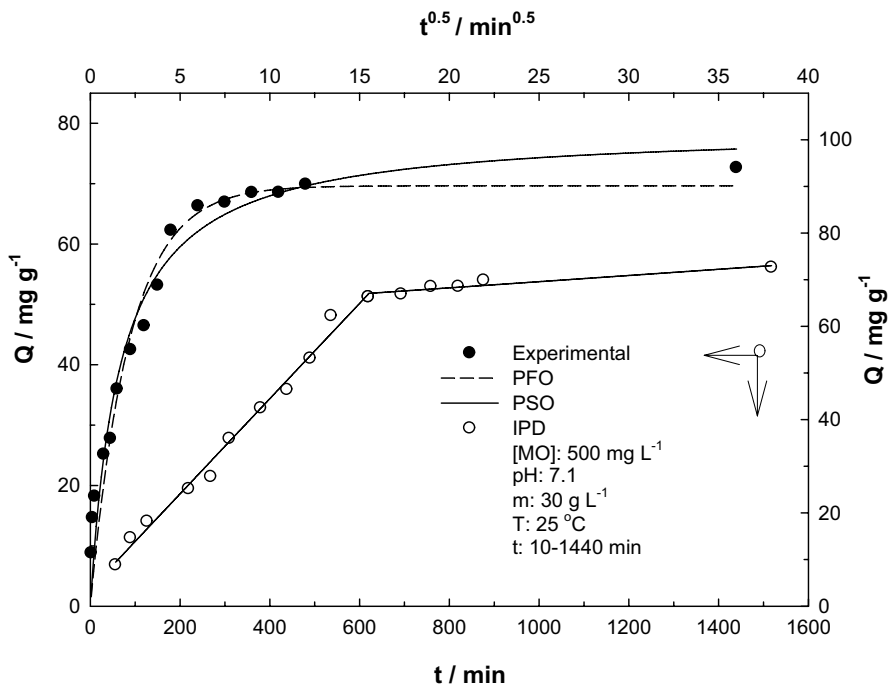

Fig. 8 Compatibility of MO dye adsorption kinetics to PFO, PSO, and IPD models

Table 3 Kinetic parameters for MO adsorbed on Ch–B composite

Kinetic model	Equation	Parameter	Value
PFO	$Q_t = Q_e\left[1 - e^{-k_1 t}\right]$	$Q_t/\text{mg g}^{-1}$	72.6
		$Q_e/\text{mg g}^{-1}$	69.6
		$k_1 \times 10^3/\text{min}^{-1}$	12.6
		R^2	0.950
PSO	$Q_t = \dfrac{t}{\left[\frac{1}{k_2 Q_e^2}\right]+\left[\frac{t}{Q_e}\right]}$	$Q_t/\text{mg g}^{-1}$	72.6
		$Q_e/\text{mg g}^{-1}$	73.4
		$k_2 \times 10^3/\text{mg}^{-1}\text{ g min}^{-1}$	0.223
		R^2	0.961
IPD	$Q_t = k_i t^{0.5}$	$k_i \times 10^3/\text{mg g}^{-1}\text{ min}^{-0.5}$	3676
		R^2	0.990

Standard deviation 22.3 mg g^{-1}, standard error 5.57 mg g^{-1}

Additionally, the IPD model was applied to the experimental data to elucidate the adsorption mechanism in MO dye removal using Ch–B composite adsorbent. The fact that the IPD model fit graph in Fig. 8 shows lines that do not pass through the origin shows that the adsorption process cannot be explained by a single mechanism and that the adsorption process involves various mechanisms. The fact that the first straight line in the IPD model fit graph does not pass through the origin shows that the adsorption process is not only limited to surface adsorption but is also controlled by IPD.

Adsorption thermodynamics

Thermodynamic parameters such as standard Gibbs free energy change ($\Delta G°$), enthalpy change ($\Delta H°$), and entropy change ($\Delta S°$) were calculated using the following equations [70].

$$K_d = \frac{Q}{C_e} \tag{5}$$

$$\Delta G° = -RT \ln\left(K_d\right) \tag{6}$$

$$\ln K_D = \frac{\Delta S°}{R} - \frac{\Delta H°}{RT} \tag{7}$$

$$\Delta G° = \Delta H° - T\Delta S° \tag{8}$$

The Van't Hoff graph showing the relationship between the equilibrium constant and temperature for the adsorption of MO dye molecules on the Ch–B composite is presented in Fig. 9, and the parameters derived from this graph are presented in Table 4. $\Delta H°$ and $\Delta S°$ were calculated from the slope and shift value of the line obtained from the Van't Hoff (ln K_D and 1/T) graph. $\Delta H°$ for MO dye removal using
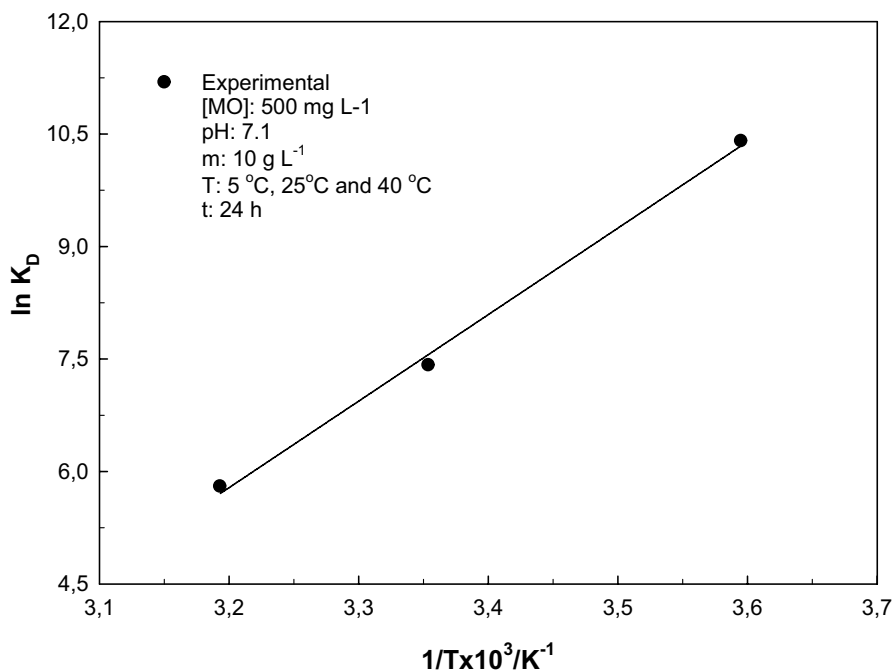
Fig. 9 The effect of temperature on the adsorption of MO dye onto Ch–B composite

Table 4 Thermodynamic parameters for MO adsorbed on Ch–B

Temperature (°C)	$\Delta G°$ (kJ mol^{-1})	$\Delta H°$ (kJ mol^{-1})	$\Delta S°$ (Jmol^{-1} K^{-1})	R^2
5	− 23.9	− 95.9	− 259	0.997
25	− 18.7			
40	− 14.8			

Ch–B composite was found to be − 95.9 kJ mol^{-1}, indicating that the reaction was exothermic. $\Delta S°$ was calculated as − 259 J mol^{-1} K^{-1} and showed that the MO dye molecules at the interface were more ordered than those in the solution phase. $\Delta G°$ values, which show that the adsorption process occurs spontaneously, were calculated as − 23.9 kJ mol^{-1} at 5 °C, − 18.7 kJ mol^{-1} at 25 °C and − 14.8 kJ mol^{-1} at 40 °C. While the negative $\Delta G°$ value showed that adsorption occurred spontaneously, the increase in $\Delta G°$ value with increasing temperature showed that adsorption was more applicable at low temperatures [71].

Desorption

Desorption, the process of releasing adsorbed molecules from a surface, is a crucial aspect of studying adsorption processes [72, 73]. In the context of a Ch–B

composite used for removing MO, understanding desorption is vital for several reasons: regeneration of the adsorbent, process efficiency, environmental implications, optimizing desorption conditions, and understanding adsorption mechanisms. Four desorbing agents are used for the desorption of MO from the Ch–B composite, such as HCl (1 mol L^{-1}), NaOH (1 mol L^{-1}), HNO$_3$ (1 mol L^{-1}), and ethyl alcohol (1 mol L^{-1}). Over 79% desorption of MO was obtained from the Ch–B studied with HNO$_3$ (Fig. 10). However, future works need various chemical, chitosan, ionic liquid, and nanoparticle treatments of cotton materials, targeted at higher uptake for common dye water pollutants.

Computational calculations

DFT study

Recently, quantum chemical calculations based on DFT theory have been employed to investigate the influence of molecular structure on the adsorption process of MO on the surface of an adsorbent. Figure 11 displays the optimized neutral and protonated forms of the MO molecule, along with their corresponding HOMO/LUMO frontier orbitals and molecular electrostatic potential maps. Specifically, the HOMO orbitals of both MO and MO–H$^+$ are situated on the rings of heterocyclic atoms and nitrogen atoms, while the LUMO orbital of the MO form is located on the aromatic ring atoms and nitrogen. In contrast, the LUMO orbital of the protonated form is
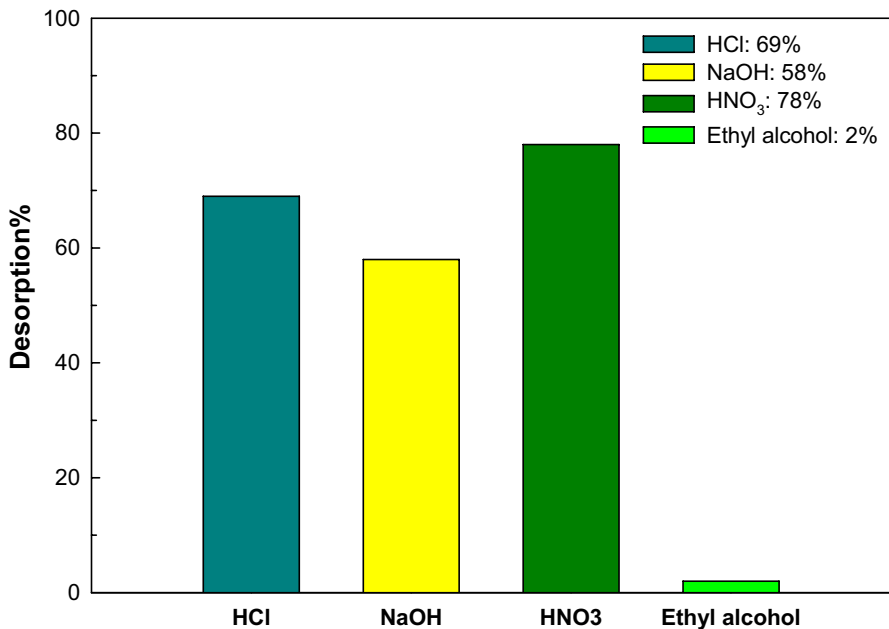

Fig. 10 The effect of desorption on Ch–B beads

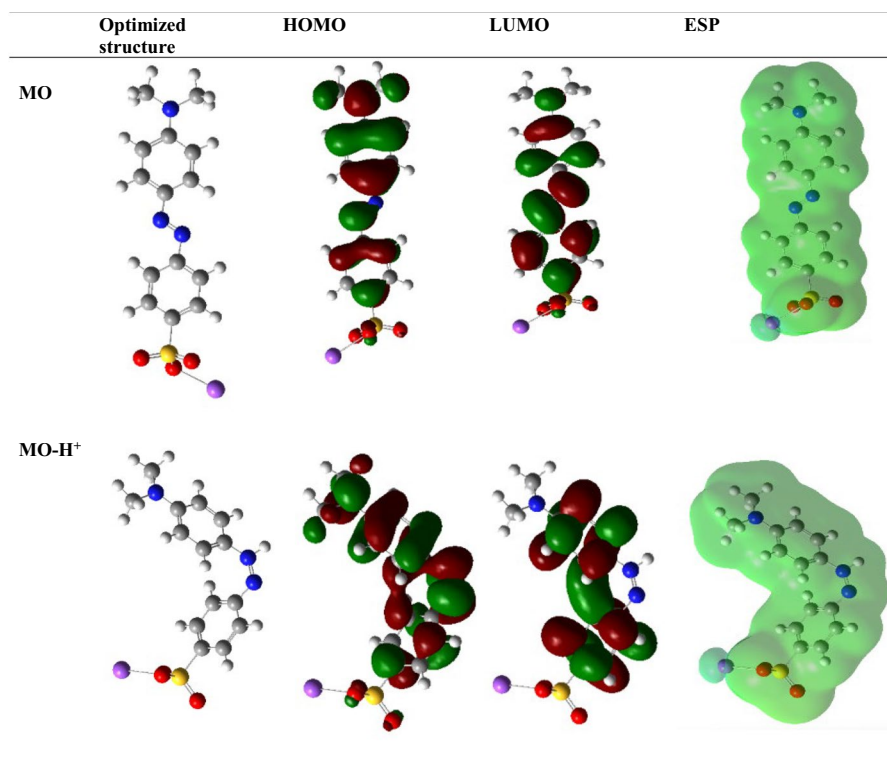|	Optimized structure	HOMO	LUMO	ESP
MO				
MO–H⁺				

Fig. 11 The pictures of optimized structures, HOMO, LUMO, and ESP

located solely on the aromatic ring atom, suggesting that the nitrogen atom may play a crucial role in the adsorption process.

To gain a better understanding of the adsorption process of the MO molecule, the HOMO, LUMO, and ΔE_{GAP} energies of both the neutral and protonated forms were computed and are summarized in Table 5. The total energy (E_{Tot}) values, which can be used to measure a molecule's reactivity and stability, were found

Table 5 Quantum chemical parameters of MO, MO–H⁺ at DFT/B3LYP 6–31G(d,p)

Quantum chemical descriptor	MO	MO–H⁺
E_{Tot} (u.a)	− 1492.6	− 1493.2
E_{HOMO} (eV)	− 5497	− 4.739
E_{LUMO} (eV)	− 2.476	− 0.724
ΔE_{GAP} (eV)	3.021	4.015
μ (eV)	− 3.987	− 2.731
χ (eV)	3.987	2.731
η (eV)	1.510	2.007
σ (eV^{-1})	0.662	0.498

to be nearly identical for both forms of the MO molecule. A low total energy value suggests low chemical stability and a high affinity for adsorption [74]. The gap energy value of the neutral MO molecule was found to be lower than that of the protonated form, indicating that the former is more prone to adsorption on the surface of Ch–B and exhibits high reactivity [75]. A negative chemical potential (μ) value (-3.987 eV for MO and -2.731 eV for MO–H$^+$) indicates stronger interaction between the dye molecules and the surface of Ch–B, suggesting favorable adsorption. A comparison of electronegativity (χ) values between the MO (3.987 eV) and MO–H$^+$ (2.731 eV) can indicate whether the adsorption process involves electron transfer or electrostatic interactions. High hardness η values indicate greater stability of the adsorption complex, suggesting strong interactions between the MO dye and Ch–B composite. Softness (σ) values (0.662 eV^{-1} for MO and 0.498 eV^{-1} for MO–H$^+$) suggest greater polarizability and flexibility, which may influence the adsorption behavior, especially in cases where the dye molecule undergoes structural changes upon adsorption. As a result, the adsorption process is expected to be highly durable.

Mulliken charges

Figure 12 displays the Mulliken charges for MO and MO–H$^+$. It is evident from these results that all heteroatoms have negative charges with high electron densities, which act as nucleophilic centers when interacting with Ch–B. As shown in Fig. 12, all nitrogen and oxygen atoms have a considerable excess of a negative charge, while some carbon atoms also have negative charges and are therefore considered active Ch–B atoms. DFT allows for a detailed examination of hydrogen bonding and electrostatic interactions between the Ch–B and MO. The identification of hydrogen bond formation and electrostatic forces provides insights into the nature of the adsorption process. These interactions play a pivotal role in stabilizing the adsorbed complex, influencing the overall adsorption energy.
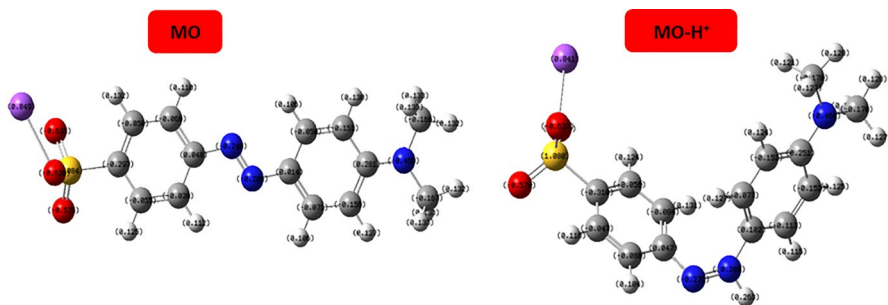

Fig. 12 Mulliken charge for the MO and MO–H$^+$ forms

Conclusion

In conclusion, this research endeavors to elucidate the intricate interplay between a Ch–B composite and MO molecules in aqueous solutions through combined theoretical and experimental investigations. The synthesis and characterization techniques employed, validate the structural and morphological aspects of the composite, confirming its suitability for adsorption studies. The experimental findings demonstrate the effective removal of MO using Ch–B, emphasizing its potential as an environmentally friendly material for water treatment applications. The integration of DFT theoretical analysis and experimental observations establishes a comprehensive framework for understanding the complex interactions governing the adsorption phenomenon. DFT calculations successfully predict the nature of molecular forces, such as hydrogen bonding and electrostatic interactions, contributing to the adsorption process. The alignment between theoretical predictions and experimental data enhances the credibility of the study and provides a robust foundation for future advancements in material design and water treatment technologies. This interdisciplinary approach not only advances our fundamental understanding of the Ch–B but also underscores the importance of bridging theoretical insights with practical applications. The synthesized composite, with its demonstrated efficiency in MO removal, holds promise for broader implications in the realm of wastewater treatment. As we navigate the challenges posed by water pollution, the sustainable and effective nature of the Ch–B composite positions them as viable candidates for eco-friendly remediation strategies, contributing to the ongoing quest for sustainable water management.

Declarations

References

1. da Silva RJ, Mojica-Sánchez LC, Gorza FDS, Pedro GC, Maciel BG, Ratkovski GP, da Rocha HD, do Nascimento KTO, Medina-Llamas JC, Chávez-Guajardo AE, Alcaraz-Espinoza JJ, de Melo CP (2021) Kinetics and thermodynamic studies of methyl orange removal by polyvinylidene fluoride-PEDOT mats. J Environ Sci. https://doi.org/10.1016/j.jes.2020.04.034
2. Iwuozor KO, Ighalo JO, Emenike EC, Ogunfowora LA, Igwegbe CA (2021) Adsorption of methyl orange: a review on adsorbent performance. Curr Res Green Sustain Chem. https://doi.org/10.1016/j.crgsc.2021.100179
3. Zhou L, Jin J, Liu Z, Liang X, Shang C (2011) Adsorption of acid dyes from aqueous solutions by the ethylenediamine-modified magnetic chitosan nanoparticles. J Hazard Mater. https://doi.org/10.1016/j.jhazmat.2010.10.012
4. el Kaim Billah R, Zaghloul A, Ahsaine HA, BaQais A, Khadoudi I, El Messaoudi N, Agunaou M, Soufiane A, Jugade R (2022) Methyl orange adsorption studies on glutaraldehyde cross-linking chitosan/fluorapatite-based natural phosphate composite. Int J Environ Anal Chem. https://doi.org/10.1080/03067319.2022.2130690
5. Wang Y, Feng W, Li J, You Z (2023) Facile one-step synthesis of CuZN–HDS/alginate hydrogel beads for highly efficient and selective removal of methyl orange. Colloids Surf A Physicochem Eng Asp. https://doi.org/10.1016/j.colsurfa.2023.131561
6. Maniyam MN, Yaacob NS, Azman HH, Ab Ghaffar NA, Abdullah H (2018) Immobilized cells of Rhodococcus strain UCC 0004 as source of green biocatalyst for decolorization and biodegradation of methyl orange. Biocatal Agric Biotechnol. https://doi.org/10.1016/j.bcab.2018.10.008
7. Alyasi H, Mackey H, McKay G (2023) Adsorption of methyl orange from water using chitosan bead-like materials. Molecules. https://doi.org/10.3390/molecules28186561
8. Gautam I, Grady T, Fernando H (2023) Degradation of the dye methyl orange using cow and goat milk iron nanoparticles. Green Chem Lett Rev. https://doi.org/10.1080/17518253.2023.2174818
9. Farhan Hanafi M, Sapawe N (2020) A review on the water problem associated with organic pollutants derived from phenol, methyl orange, and remazol brilliant blue dyes. Mater Today Proc 31:A141–A150. https://doi.org/10.1016/j.matpr.2021.01.258
10. El Messaoudi N, El Khomri M, Goodarzvand Chegini Z, Chlif N, Dbik A, Bentahar S, Iqbal M, Jada A, Lacherai A (2023) Desorption study and reusability of raw and H_2SO_4 modified jujube shells (*Zizyphus lotus*) for the methylene blue adsorption. Int J Environ Anal Chem. https://doi.org/10.1080/03067319.2021.1912338
11. Narwal N, Katyal D, Kataria N, Rose PK, Warkar SG, Pugazhendhi A, Ghotekar S, Khoo KS (2023) Emerging micropollutants in aquatic ecosystems and nanotechnology-based removal alternatives: a review. Chemosphere. https://doi.org/10.1016/j.chemosphere.2023.139945
12. Sharma J, Sharma S, Soni V (2021) Classification and impact of synthetic textile dyes on aquatic flora: a review. Reg Stud Mar Sci. https://doi.org/10.1016/j.rsma.2021.101802
13. Tahir U, Yasmin A, Khan UH (2016) Phytoremediation: potential flora for synthetic dyestuff metabolism. J King Saud Univ Sci. https://doi.org/10.1016/j.jksus.2015.05.009
14. Lellis B, Fávaro-Polonio CZ, Pamphile JA, Polonio JC (2019) Effects of textile dyes on health and the environment and bioremediation potential of living organisms. Biotechnol Res Innov. https://doi.org/10.1016/j.biori.2019.09.001
15. Al-Tohamy R, Ali SS, Li F, Okasha KM, Mahmoud YAG, Elsamahy T, Jiao H, Fu Y, Sun J (2022) A critical review on the treatment of dye-containing wastewater: ecotoxicological and health concerns of textile dyes and possible remediation approaches for environmental safety. Ecotoxicol Environ Saf. https://doi.org/10.1016/j.ecoenv.2021.113160
16. El Khomri M, El Messaoudi N, Dbik A, Bentahar S, Fernine Y, Lacherai A, Jada A (2022) Optimization based on response surface methodology of anionic dye desorption from two agricultural solid wastes. Chem Afr. https://doi.org/10.1007/s42250-022-00395-4
17. İlyasoglu G, Kose-Mutlu B, Mutlu-Salmanli O, Koyuncu I (2022) Removal of organic micropollutans by adsorptive membrane. Chemosphere. https://doi.org/10.1016/j.chemosphere.2022.134775
18. Mulay MR, Martsinovich N (2022) Water pollution and advanced water treatment technologies. Palgrave Encycl Urban Reg Futures. https://doi.org/10.1007/978-3-030-87745-3_189
19. Mota LSO, de Oliveira PCO, Peixoto BS, de Moraes MC (2023) Enzyme-coated biochar as a sustainable solution for water and wastewater treatment. Environ Sci Water Res Technol. https://doi.org/10.1039/d3ew00074e

20. Saravanan A, Senthil Kumar P, Jeevanantham S, Karishma S, Tajsabreen B, Yaashikaa PR, Reshma B (2021) Effective water/wastewater treatment methodologies for toxic pollutants removal: processes and applications towards sustainable development. Chemosphere. https://doi.org/10.1016/j.chemosphere.2021.130595

21. Gupta VK (2009) Application of low-cost adsorbents for dye removal—a review. J Environ Manag. https://doi.org/10.1016/j.jenvman.2008.11.017

22. El Messaoudi N, El Khomri M, Dbik A, Bentahar S, Lacherai A (2017) Selective and competitive removal of dyes from binary and ternary systems in aqueous solutions by pretreated jujube shell (*Zizyphus lotus*). J Dispers Sci Technol. https://doi.org/10.1080/01932691.2016.1228070

23. Dehghani MH, Ahmadi S, Ghosh S, Othmani A, Osagie C, Meskini M, AlKafaas SS, Malloum A, Khanday WA, Jacob AO, Gökkuş Ö, Oroke A, Martins Chineme O, Karri RR, Lima EC (2023) Recent advances on sustainable adsorbents for the remediation of noxious pollutants from water and wastewater: a critical review. Arab J Chem. https://doi.org/10.1016/j.arabjc.2023.105303

24. Swain J, Priyadarshini A, Hajra S, Panda S, Panda J, Samantaray R, Yamauchi Y, Han M, Kim HJ, Sahu R (2023) Photocatalytic dye degradation by $BaTiO_3$/zeolitic imidazolate framework composite. J Alloys Compd. https://doi.org/10.1016/j.jallcom.2023.171438

25. Hisham F, Maziati Akmal MH, Ahmad F, Ahmad K, Samat N (2024) Biopolymer chitosan: potential sources, extraction methods, and emerging applications. Ain Shams Eng J. https://doi.org/10.1016/j.asej.2023.102424

26. Piekarska K, Sikora M, Owczarek M, Jóźwik-Pruska J, Wiśniewska-Wrona M (2023) Chitin and chitosan as polymers of the future-obtaining, modification, life cycle assessment and main directions of application. Polym 15:793. https://doi.org/10.3390/POLYM15040793

27. Kahr G, Madsen FT (1995) Determination of the cation exchange capacity and the surface area of bentonite, illite and kaolinite by methylene blue adsorption. Appl Clay Sci. https://doi.org/10.1016/0169-1317(94)00028-O

28. Bohác P, Delavernhe L, Zervas E, Königer F, Schuhmann R, Emmerich K (2019) Cation exchange capacity of bentonite in a saline environment. Appl Geochem. https://doi.org/10.1016/j.apgeochem.2018.12.019

29. Frisch MJ, Trucks GW, Schlegel HB, Scuseria GE, Robb MA, Cheeseman JR, Scalmani G, Barone V, Mennucci B, Petersson GA, Nakatsuji H, Caricato M, Li X, Hratchian HP, Izmaylov AF, Bloino J, Zheng G, Sonnenberg JL, Hada M, Ehara M, Toyota K, Fukuda R, Hasegawa J, Ishida M, Nakajima T, Honda Y, Kitao O, Nakai H, Vreven T, Montgomery JA Jr, Peralta JE, Ogliaro F, Bearpark M, Heyd JJ, Brothers E, Kudin KN, Staroverov VN, Kobayashi R, Normand J, Raghavachari K, Rendell A, Burant JC, Iyengar SS, Tomasi J, Cossi M, Rega N, Millam JM, Klene M, Knox JE, Cross JB, Bakken V, Adamo C, Jaramillo J, Gomperts R, Stratmann RE, Yazyev O, Austin AJ, Cammi R, Pomelli C, Ochterski JW, Martin RL, Morokuma K, Zakrzewski VG, Voth GA, Salvador P, Dannenberg JJ, Dapprich S, Daniels AD, Farkas, Foresman JV, Ortiz J, Cioslowski J, Fox DJ (2010) Gaussian09 Revision D.01. Gaussian Inc., Wallingford

30. Aziz SB, Hamsan MH, Karim WO, Kadir MFZ, Brza MA, Abdullah OG (2019) High proton conducting polymer blend electrolytes based on chitosan: dextran with constant specific capacitance and energy density. Biomolecules. https://doi.org/10.3390/biom9070267

31. Zhirong L, Azhar Uddin M, Zhanxue S (2011) FT-IR and XRD analysis of natural Na-bentonite and Cu(II)-loaded Na-bentonite. Spectrochim Acta Part A Mol Biomol Spectrosc. https://doi.org/10.1016/j.saa.2011.04.013

32. Ertap H, Karabulut M (2019) Structural and electrical properties of boron doped InSe single crystals. Mater Res Express. https://doi.org/10.1088/2053-1591/aaf2f6

33. Pawlak A, Mucha M (2003) Thermogravimetric and FTIR studies of chitosan blends. Thermochim Acta. https://doi.org/10.1016/S0040-6031(02)00523-3

34. Lawrie G, Keen I, Drew B, Chandler-Temple A, Rintoul L, Fredericks P, Grøndahl L (2007) Interactions between alginate and chitosan biopolymers characterized using FTIR and XPS. Biomacromol. https://doi.org/10.1021/bm070014y

35. Alabarse FG, Conceição RV, Balzaretti NM, Schenato F, Xavier AM (2011) In-situ FTIR analyses of bentonite under high-pressure. Appl Clay Sci. https://doi.org/10.1016/j.clay.2010.11.017

36. Yang J, Huang B, Lin M (2020) Adsorption of hexavalent chromium from aqueous solution by a chitosan/bentonite composite: isotherm, kinetics, and thermodynamics studies. J Chem Eng Data. https://doi.org/10.1021/acs.jced.0c00085

37. Şenol ZM, Şimşek S (2022) Insights into effective adsorption of lead ions from aqueous solutions by using chitosan-bentonite composite beads. J Polym Environ. https://doi.org/10.1007/s10924-022-02464-8

38. Fernine Y, Arrousse N, Haldhar R, Raorane CJ, Kim SC, El Hajjaji F, Touhami ME, Beniken M, Haboubi K, Taleb M (2022) Synthesis and characterization of phenolphthalein derivatives, detailed theoretical DFT computation/molecular simulation, and prevention of AA2024-T3 corrosion in medium 3.5% NaCl. J Taiwan Inst Chem Eng. https://doi.org/10.1016/j.jtice.2022.104556

39. Shearer L, Pap S, Gibb SW (2022) Removal of pharmaceuticals from wastewater: a review of adsorptive approaches, modelling and mechanisms for metformin and macrolides. J Environ Chem Eng. https://doi.org/10.1016/j.jece.2022.108106

40. El Khomri M, El Messaoudi N, Dbik A, Bentahar S, Fernine Y, Bouich A, Lacherai A, Jada A (2022) Modification of low-cost adsorbent prepared from agricultural solid waste for the adsorption and desorption of cationic dye. Emergent Mater 5:1679–1688. https://doi.org/10.1007/S42247-022-00390-Y

41. Cheruiyot GK, Wanyonyi WC, Kiplimo JJ, Maina EN (2019) Adsorption of toxic crystal violet dye using coffee husks: equilibrium, kinetics and thermodynamics study. Sci Afr. https://doi.org/10.1016/j.sciaf.2019.e00116

42. Uddin MT, Rahman MA, Rukanuzzaman M, Islam MA (2017) A potential low cost adsorbent for the removal of cationic dyes from aqueous solutions. Appl Water Sci. https://doi.org/10.1007/s13201-017-0542-4

43. El Khomri M, El Messaoudi N, Dbik A, Bentahar S, Lacherai A, Chegini ZG, Bouich A (2022) Removal of congo red from aqueous solution in single and binary mixture systems using argan nutshell wood. Pigment Resin Technol 51:477–488. https://doi.org/10.1108/PRT-04-2021-0045

44. Şenol ZM (2021) A chitosan-based composite for adsorption of uranyl ions; mechanism, isothems, kinetics and thermodynamics. Int J Biol Macromol 183:1640–1648. https://doi.org/10.1016/j.ijbiomac.2021.05.130

45. Lafi R, Hafiane A (2016) Removal of methyl orange (MO) from aqueous solution using cationic surfactants modified coffee waste (MCWs). J Taiwan Inst Chem Eng. https://doi.org/10.1016/j.jtice.2015.06.035

46. Kamaru AA, Sani NS, Malek NANN (2016) Raw and surfactant-modified pineapple leaf as adsorbent for removal of methylene blue and methyl orange from aqueous solution. Desalin Water Treat. https://doi.org/10.1080/19443994.2015.1095122

47. Yu J, Zhang X, Wang D, Li P (2018) Adsorption of methyl orange dye onto biochar adsorbent prepared from chicken manure. Water Sci Technol. https://doi.org/10.2166/wst.2018.003

48. Munagapati VS, Yarramuthi V, Kim DS (2017) Methyl orange removal from aqueous solution using goethite, chitosan beads and goethite impregnated with chitosan beads. J Mol Liq. https://doi.org/10.1016/j.molliq.2017.05.099

49. Zayed AM, Abdel Wahed MSM, Mohamed EA, Sillanpää M (2018) Insights on the role of organic matters of some Egyptian clays in methyl orange adsorption: isotherm and kinetic studies. Appl Clay Sci. https://doi.org/10.1016/j.clay.2018.09.013

50. Martinez MV, Molina M, Barbero CA (2018) Poly(N-isopropylacrylamide) cross-linked gels as ıntrinsic amphiphilic materials: swelling properties used to build novel ınterphases. J Phys Chem B. https://doi.org/10.1021/acs.jpcb.8b07625

51. Xing X, Chang PH, Lv G, Jiang WT, Jean JS, Liao L, Li Z (2016) Ionic-liquid-crafted zeolite for the removal of anionic dye methyl orange. J Taiwan Inst Chem Eng. https://doi.org/10.1016/j.jtice.2015.07.026

52. Radoor S, Karayil J, Jayakumar A, Parameswaranpillai J, Siengchin S (2021) Efficient removal of methyl orange from aqueous solution using mesoporous ZSM-5 zeolite: synthesis, kinetics and isotherm studies. Colloids Surf A Physicochem Eng Asp. https://doi.org/10.1016/j.colsurfa.2020.125852

53. Lafi R, Abdellaoui L, Montasser I, Hafiane A (2022) Removal of methyl orange from aqueous solution onto modified extracted cellulose from *Stipa tenacissima* L. Int J Environ Anal Chem. https://doi.org/10.1080/03067319.2020.1845663

54. Kang D, Yu X, Ge M, Xiao F, Xu H (2017) Novel Al-doped carbon nanotubes with adsorption and coagulation promotion for organic pollutant removal. J Environ Sci (China). https://doi.org/10.1016/j.jes.2016.04.022

55. Uddin MK, Baig U (2019) Synthesis of Co_3O_4 nanoparticles and their performance towards methyl orange dye removal: characterisation, adsorption and response surface methodology. J Clean Prod. https://doi.org/10.1016/j.jclepro.2018.11.232

56. Debnath A, Deb K, Chattopadhyay KK, Saha B (2016) Methyl orange adsorption onto simple chemical route synthesized crystalline α-Fe_2O_3 nanoparticles: kinetic, equilibrium isotherm, and neural network modeling. Desalin Water Treat. https://doi.org/10.1080/19443994.2015.1060540

57. Banerjee D, Bhowmick P, Pahari D, Santra S, Sarkar S, Das B, Chattopadhyay KK (2017) Pseudo first ordered adsorption of noxious textile dyes by low-temperature synthesized amorphous carbon nanotubes. Phys E Low Dimens Syst Nanostruct. https://doi.org/10.1016/j.physe.2016.11.024

58. Kundu S, Chowdhury IH, Naskar MK (2017) Synthesis of hexagonal shaped nanoporous carbon for efficient adsorption of methyl orange dye. J Mol Liq. https://doi.org/10.1016/j.molliq.2017.03.090

59. Fan J, Zhao Z, Liu W, Xue Y, Yin S (2016) Solvothermal synthesis of different phase N–TiO_2 and their kinetics, isotherm and thermodynamic studies on the adsorption of methyl orange. J Colloid Interface Sci. https://doi.org/10.1016/j.jcis.2016.02.045

60. Istratie R, Stoia M, Păcurariu C, Locovei C (2019) Single and simultaneous adsorption of methyl orange and phenol onto magnetic iron oxide/carbon nanocomposites. Arab J Chem. https://doi.org/10.1016/j.arabjc.2015.12.012

61. Wong S, Tumari HH, Ngadi N, Mohamed NB, Hassan O, Mat R, Saidina Amin NA (2019) Adsorption of anionic dyes on spent tea leaves modified with polyethyleneimine (PEI-STL). J Clean Prod. https://doi.org/10.1016/j.jclepro.2018.09.201

62. Mirzaei D, Zabardasti A, Mansourpanah Y, Sadeghi M, Farhadi S (2020) Efficacy of novel NaX/MgO–TiO_2 zeolite nanocomposite for the adsorption of methyl orange (MO) dye: ısotherm, kinetic and thermodynamic studies. J Inorg Organom Polym Mater. https://doi.org/10.1007/s10904-019-01369-9

63. Bahrudin NN, Nawi MA, Jawad AH, Sabar S (2020) Adsorption characteristics and mechanistic study of ımmobilized chitosan-montmorillonite composite for methyl orange removal. J Polym Environ. https://doi.org/10.1007/s10924-020-01734-7

64. Hussain S, Kamran M, Khan SA, Shaheen K, Shah Z, Suo H, Khan Q, Shah AB, Rehman WU, Al-Ghamdi YO, Ghani U (2021) Adsorption, kinetics and thermodynamics studies of methyl orange dye sequestration through chitosan composites films. Int J Biol Macromol. https://doi.org/10.1016/j.ijbiomac.2020.12.054

65. Huang R, Liu Q, Huo J, Yang B (2017) Adsorption of methyl orange onto protonated cross-linked chitosan. Arab J Chem. https://doi.org/10.1016/j.arabjc.2013.05.017

66. Zhai L, Bai Z, Zhu Y, Wang B, Luo W (2018) Fabrication of chitosan microspheres for efficient adsorption of methyl orange. Chin J Chem Eng. https://doi.org/10.1016/j.cjche.2017.08.015

67. Zhang L, Liu Q, Hu P, Huang R (2016) Adsorptive removal of methyl orange using enhanced cross-linked chitosan/bentonite composite. Desalin Water Treat. https://doi.org/10.1080/19443994.2015.1088478

68. Bulin C, Guo T, Zheng R, Xiong Q (2024) Interaction mechanism of phytic acid functionalized graphene oxide with ionic dyes. Sep Purif Technol. https://doi.org/10.1016/j.seppur.2023.125369

69. Bulin C (2023) Adsorption mechanism and removal efficiency of magnetic graphene oxide-chitosan hybrid on aqueous Zn(II). Int J Biol Macromol. https://doi.org/10.1016/j.ijbiomac.2023.124588

70. Şenol ZM, El Messaoudi N, Fernine Y, Keskin ZS (2023) Bioremoval of rhodamine B dye from aqueous solution by using agricultural solid waste (almond shell): experimental and DFT modeling studies. Biomass Convers Biorefin. https://doi.org/10.1007/s13399-023-03781-1

71. El Mouden A, El Messaoudi N, El Guerraf A, Bouich A, Mehmeti V, Lacherai A, Jada A, Pinê Américo-Pinheiro JH (2023) Removal of cadmium and lead ions from aqueous solutions by novel dolomite-quartz@Fe_3O_4 nanocomposite fabricated as nanoadsorbent. Environ Res 225:115606. https://doi.org/10.1016/J.ENVRES.2023.115606

72. Aljeboree AM, Radia ND, Jasim LS, Alwarthan AA, Khadhim MM, Washeel Salman A, Alkaim AF (2022) Synthesis of a new nanocomposite with the core TiO_2/hydrogel: brilliant green dye adsorption, isotherms, kinetics, and DFT studies. J Ind Eng Chem. https://doi.org/10.1016/j.jiec.2022.02.031

73. Sočo E, Domoń A, Papciak D, Michel MM, Pająk D, Cieniek B, Azizi M (2023) Characteristics of adsorption/desorption process on dolomite adsorbent in the copper(II) removal from aqueous solutions. Materials (Basel). https://doi.org/10.3390/ma16134648

74. Somashekara D, Mulky L (2023) Sequestration of contaminants from wastewater: a review of adsorption processes. ChemBioEng Rev. https://doi.org/10.1002/cben.202200050

75. Fernine Y, Salim R, Arrousse N, Haldhar R, El Hajjaji F, Kim SC, Ebn Touhami M, Taleb M (2022) Anti-corrosion performance of Ocimum basilicum seed extract as environmental friendly inhibitors for mild steel in HCl solution: evaluations of electrochemical, EDX, DFT and Monte Carlo. J Mol Liq. https://doi.org/10.1016/j.molliq.2022.118867